Is there a global carbonate layer in the oceanic mantle?

Tahar Hammouda, Geeth Manthilake, P. Goncalves, Julien Chantel, J. Guignard, W. Crichton, Fabrice Gaillard

Is there a global carbonate layer in the oceanic mantle?

T. HAMMOUDA[1], G. MANTHILAKE[1], P. GONCALVES[2], J. CHANTEL[1,3]*, J. GUIGNARD[4]†, W. CRICHTON[4], and F. GAILLARD[5]

[1]Laboratoire Magmas et Volcans, Université Clermont-Auvergne, 6 avenue Blaise Pascal, 63178 Aubière, France

[2]UMR 6249 Chrono-environnement, Université de Bourgogne Franche-Comté, France

[3]Department of Earth, Environmental, and Planetary Sciences, Case Western Reserve University, Cleveland, OH 44106, USA

[4]ESRF, 71 avenue des Martyrs, F-38000 Grenoble, France

[5]ISTO, 5 rue de la Férollerie, F-45100 Orléans cedex 2, France

Corresponding author: Tahar Hammouda (tahar.hammouda@uca.fr)

*now at Unité Matériaux et Transformations, Université Lille1, 59655 Villeneuve d'Ascq France.

†now at Géosciences Environnement Toulouse (GET), OMP-UPS-CNRS, 14 Avenue E. Belin, 31400 Toulouse, France.

Key Points:

- CO_2 release during subduction and its transfer to the mantle initiates compression melting at the lithosphere-asthenosphere boundary.
- Dissolution-precipitation driven melt porous flow results in migration of carbonatite melt away from the mantle wedge.
- Steady supply of carbonated material by subduction may build up a global carbonatite melt layer at the top of the oceanic asthenosphere.

Abstract

Previous modeling of carbonate subduction by high-pressure experimentation has allowed to propose scenarios for bulk carbon return to the mantle, but the detailed transfer mechanisms have seldom been studied. We monitored carbonate – silicate reactions by combining high-pressure experiments and synchrotron-based x-ray diffraction. Carbonates break down at moderate pressure and high temperature and CO_2 is trapped at grain boundaries. Further isothermal compression yields melting, which may control continuous carbon introduction, first in the mantle wedge, and next, away from the wedge. Carbon presence has been discussed in a variety of magmatic contexts, under the oceanic lithosphere (hotspots, petit spots, fossil ridges). We suggest the presence of a global carbon-rich layer under the oceanic lithosphere that is steadily fed by subduction processes. This layer can be the source of mechanical weakening of the lithosphere-asthenosphere boundary under the oceans. Therefore, carbon-induced compression melting may be a key mechanism of modern-style plate tectonics.

Plain Language Summary

Plate tectonics, the mechanism by which rigid plates migrate atop the Earth's mantle, necessitate mechanical decoupling between the plates (lithosphere) and the underlying mantle (asthenosphere). The presence of a melt layer acting as a lubricating agent has been discussed on the basis of geophysical evidence, such as provided by seismic and electrical conductivity data analysis. In this study, we show that this layer can be fueled by the melting of carbonate-rich material carried down by oceanic plates returning to the mantle at subduction zones. This process is continuous because the Earth is an active planet with permanent seismic and volcanic activity. It may have been going on for billions of years and may have been fundamental for the initiation of plate tectonics.

1 Introduction

Continuous volcanic activity causes the escape of volatiles from the mantle. This degassing process is partly counterbalanced by the recycling of volatiles at subduction zones, including water, carbon dioxide, and noble gases (Poli & Schmidt, 1995; Zhang & Zindler, 1993; Sleep et al., 2012; Jackson et al., 2013). Volatile compounds are introduced in the mantle with altered oceanic crust at subduction zones.

Previous studies showed that breakdown of water- and hydroxyl-bearing minerals releases important quantities of water-rich fluids at depths corresponding to fore-arc to back-arc regions (Schmidt & Poli, 1995). However, the importance of CO_2-rich fluids is increasingly recognized and CO_2 may be as important as H_2O in petrogenetic processes (Molina & Poli, 2000; Gorman et al., 2006). CO_2-rich fluid released from the slab may be introduced into the mantle wedge, via a complex process that could involve crack propagation, as discussed by Brenan & Watson (1988).

At depths corresponding to pressures lower than 2.5 GPa (ca. 75 km), the addition of CO_2 is not expected to cause mantle melting because the the pressure is too low for carbon to initiate melting (the carbonate ledge, as defined by Eggler, 1987). In addition, Watson et al. (1990) showed that H_2O-CO_2 mixed fluids have very poor wetting properties, even at low CO_2 content. Therefore, if present, CO_2-rich fluids do not have a tendency to form an interconnected network and cannot migrate by porous flow. This absence of mobility may be the cause of the common occurrence of CO_2 fluid inclusions in mantle minerals (Roedder, 1965, and the recent review by Frezzotti and Thouret, 2014). By remaining locked at grain boundaries, CO_2-rich fluids create CO_2-impregnated domains confined at the slab/mantle wedge interface, resulting in the formation of CO_2-enriched peridotite bodies as discussed by Scambelluri et al. (2016). Because of the viscous coupling of the plunging slab and the wedge, this modified mantle region may be entrained to greater depths. The burial of this oceanic plate-borne carbonated material is near isothermal because in this region, the isotherms are sub-parallel to the slab mantle interface (Syracuse et al., 2010).

Here we explore the outcome of having CO_2-rich fluids at the slab-mantle interface, by using high-pressure in-situ experiments combined with synchrotron radiation. Compared to quench studies, our approach allows for testing a global scenario of carbon delivery and reaction at mantle conditions by reproducing pressure-temperature path of subduction, coupled with continuous x-ray monitoring. A major point that is tackled is whether, once formed, CO_2-rich fluids escape the system or remain and act as fluxing agents at high pressure. As will be discussed, the possibility for the dissemination of carbon-bearing material at the lithosphere-asthenosphere boundary depends on the answer to this question.

2 Materials and Methods

Experiments were performed using the 2000 ton multianvil press operated on ID06 beamline of the European Synchrotron Radiation Facility, following the approach used in Hammouda et al. (2014). The details on the experimental and analytical methods are provided in the supporting-information file. We used a synthetic model system with almost purely magnesian endmember minerals. Compared to natural systems, this experimental strategy results in shifting all reaction temperatures by about 250 °C toward higher values, without changing the overall

arrangement of the phase diagram (Hammouda & Keshav, 2015). Two experimental runs are reported. The first one was designed to investigate CO_2-fluid release, whereas the second one explored further reactions involving the fluid. The latter pressure-temperature path is illustrated in Figure 1 and the corresponding x-ray diffraction patterns are shown in Figure 2.

A mixture of [enstatite + dolomite] was first compressed and heated, up to 2.25 GPa and 977°C (Figure 1). Enstatite and dolomite diffraction lines are visible on the first pattern of Figure 2. Further heating to 1100°C at about the same pressure results in dolomite diffraction line disappearing, while diopside lines start growing. If present, forsterite lines are faint. They are visible only after further heating to 1150°C. This combination of diffraction lines growth (diopside and forsterite) and collapse (dolomite) attests for crossing of the following decarbonation reaction

$$\text{Enstatite} + \text{Dolomite} = \text{Diopside} + \text{Forsterite} + CO_2.$$

The texture resulting from decarbonation, with isolated pores (previously filled with CO_2 fluid) is illustrated in Figure 3A, which presents the result of the experiment that was interrupted at this stage.

Heating up to over 1300°C results in no major change in the diffraction pattern. Further compression with the temperature kept around 1330°C yields no change up to 2.71 GPa. However, while increasing pressure from 2.71 to 3.02 GPa, diopside and forsterite diffraction lines collapse, and enstatite lines start growing (Figure 2), whereas dolomite diffraction lines were not observed. This is an indication that the melting reaction has been crossed (Figure 1). In this experiment, the melt presence is difficult to demonstrate on the sole basis of diffraction patterns. However, after the experiment was quenched, the resulting assemblage was studied by scanning electron microscopy. The corresponding texture (Figure 3B) shows evidence for melting. In this experiment the melting of a silicate + CO_2 assemblage has been directly monitored and demonstrated to occur solely as an effect of compression at constant temperature. The crossing of the solidus boundary defines the carbonate ledge (Eggler, 1978; 1987). Melting is a result of fluid CO_2 remaining trapped in the solid silicate assemblage.

3 Discussion

In our experimental simulation, the carbonatitic melt is produced at conditions corresponding to a CO_2-impregnated mantle wedge crossing the carbonate ledge. Therefore, the ledge acts as a melting curve at about 80 km depth, in the context of subduction zones. This is a situation wherein silicate + CO_2 melting occurs because of compression, at nearly isothermal conditions. Usually, melting in the mantle is associated with decompression in upwelling plumes, either at mid-ocean ridges or at hot spots, because in most cases, melting is accompanied by volume expansion. Otherwise, melting can be caused by the introduction of a fluxing agent,

such as H_2O in the case of arc magmatism. Here we illustrate an occurrence of melting associated with downwelling, because of the peculiarities of the silicate + CO_2 phase diagram.

The excellent wetting properties of carbonatitic melts (dihedral angles < 30 °, Hunter & McKenzie, 1989; Watson et al., 1990; Hammouda & Laporte, 2000) and their very low viscosity (Kono et al., 2014) at mantle conditions allow for their very efficient percolation into the surrounding melt-free mantle, provided they are not reduced to graphite (Stagno et al., 2013). Therefore, at about 80 km depth, a region of carbonated melt-impregnated mantle is formed near the slab (Figure 4). This modified mantle may be entrained to greater depths because of the coupling between the plate and the mantle. However, the melt may also spread horizontally, because carbonatitic melts have a spontaneous tendency to infiltrate the melt-free mantle by surface-energy minimization. This migration, which is driven by dissolution-precipitation, is faster than mantle flow and can operate even against gravity (Hammouda & Laporte, 2000). Decoupling between melt and mantle movement is thus expected, contrary to the CO_2 fluid-mantle situation, and a carbonatite-rich region extending far from the slab can develop in the mantle wedge and further away from the slab, at about 80 km depth. This carbonatite-rich domain is limited toward shallow levels by the ledge. It is limited toward greater depth (about 150 km) by carbon reduction (Stagno et al., 2013; Hammouda & Keshav, 2015).

On the basis of thermodynamic modeling, previous studies (Gorman et al., 2006) have shown that high CO_2 contents should be expected in fluids produced in a hot subduction environment, which is precisely the case of the Cascadia area. Here, we suggest that highly mobile carbonatitic melts, originating from the encounter of released CO_2-rich fluids with the mantle wedge peridotites are the cause of the observed high conductivity of the Cascadia subduction zone. At a larger scale, this mechanism could be responsible for delivering carbon-rich material at the base of the lithosphere, creating a shallow mantle carbon reservoir (Sleep, 2003; Kelemen & Manning). If reheated, this metasomatized mantle region could be the source of kimberlite-carbonatite magmatism such as observed in North America along a line parallel to the western paleo-subduction margin of the North American plate (Duke et al., 2014) or along the North-China craton (Chen et al., 2016). After spreading at the bottom of the lithosphere, the CO_2-bearing melts may be involved in the source of petit spots, as recently discussed by Machida et al. (2017). It may also be anticipated that carbonated material that would escape remobilization at petit spots could be buried during a later subduction event. There, carbon-enriched material is located at the back of the subducting slab (Figure 4). It is therefore separated from the hot mantle wedge by the thickness of the subducting lithosphere. This two-stage process is a much more efficient way of introducing carbon to great depth because the thermal regime is cooler than when carbon is carried on top of the plate.

The amount and composition of the fluid released by the altered oceanic crust are highly dependent on the subduction pressure-temperature regime. The recent thermo-mechanical models (Syracuse et al., 2010) point toward paths hotter than earlier estimates mainly because of the coupling between the slab and the mantle wedge. With the new models, it is possible that even cool subduction paths also allow for the release of carbon-bearing fluids. Earlier experimental studies have shown that the depth of the carbonate ledge depends only slightly on the CO_2/H_2O ratio (Hammouda & Keshav, 2015). Therefore, the presence of a layer of carbonatite-impregnated mantle wedge may be a general feature of subduction zones, assuming

that carbonated material (altered crust or sediments) is carried by the plate, which is a likely situation.

4 Conclusions

The release of CO_2 during the subduction of altered oceanic crust and its transfer to the mantle wedge initiates compression melting at the lithosphere-asthenosphere boundary. The melt formed can migrate away from the mantle wedge by porous flow driven by dissolution-precipitation at grain boundaries. Because subduction zones are continuously active on the scale of the whole planet, the steady supply of carbonated material may build up a global carbonatite melt layer at the top of the asthenosphere.

Recent petrological and geophysical investigations lend support to the presence of a carbon-rich melt layer at the oceanic lithosphere/asthenosphere boundary, away from mid-ocean ridge axes. Petrological evidence comes from the low-degree melts in spreading centers (Zhang et al., 2017), from petit spot volcanism (Machida et al., 2017) and from metasomatism in the source of hot spots (Hauri et al., 1993). Further evidence of melt presence at the lithosphere-asthenosphere boundary arises from seismic data (Schmerr, 2012) and these melt physical properties strongly suggest a carbonate-rich composition (Sifré et al., 2014). Our results show that melt trapped at this depth may originate, not only from upwelling regions (Liu et al., 2020) but also from down-going oceanic plates. This possibility is further substantiated by electrical conductivity anomalies observed in the Cascadia subduction zone (Soyer & Unsworth, 2006). So far, serpentinized mantle, caused by water-rich fluid circulation, has been invoked, but serpentine presence cannot explain high conductivity (Guo et al., 2011).

Carbonate-based sediments are present in Archean terranes, and 3.7 Ga old stromatoliths have been reported from the Isua region in Greenland (Nutman et al., 2016). Recycling of material of crustal origin in modern type subduction started at least about 3.2 billion years ago (Næraa et al., 2012). Given that the hot subduction regime was rather the rule for the young Earth, it can be anticipated that the process of sub-lithospheric impregnation by carbonate melts has been active very early in the planet history. It may have aided mechanical decoupling at the lithosphere-asthenosphere boundary, triggering modern-style plate tectonics.

Acknowledgments

This work was financially supported by the European Synchrotron Radiation Facility (ESRF proposal ES-25). Help by J.-L. Devidal on the electron microprobe and by J.-M. Hénot on the SEM are gratefully acknowledged. This research was partly supported by the French Government Laboratory of Excellence initiative n°ANR-10-LABX-0006, the Région Auvergne and the European Regional Development Fund. FG is supported by the European Research Council (ERC grant number 279790) and the French agency for research (ANR project #2010 BLAN62101). This is Laboratory of Excellence ClerVolc contribution 437.

The authors comply with AGU's data policy, and the x-ray diffraction data of this study are available in the general repository Figshare (doi:10.6084/m9.figshare.12464687). The authors declare no competing financial interests.

References

Brenan J.M., Watson E.B. (1988) Fluids in the lithosphere, 2. Experimental constraints on CO_2 transport in dunite and quartzite at elevated P-T conditions with implications for mantle and crustal decarbonation processes, *Earth and Planetary Science Letters*, 91, 141-158.

Chen, C.F., Liu, Y.S., Foley, S.F., Ducea, M.N., He, D.T., Hu, Z.C., Chen, W., Zong, K.Q. (2016) Paleo-Asian oceanic slab under the North China craton revealed by carbonatites derived from subducted limestones, *Geology*, 44 (12), 1039–1042.

Dalton J.D., Presnall D.C. (1998) Carbonatitic melts along the solidus of model lherzolite in the system CaO-MgO-Al_2O_3-SiO_2-CO_2 from 3 to 7 GPa, *Contributions to Mineralogy and Petrology*, 131, 123-135.

Duke, G.I., Carlson, R.W., Frost, C.D., Hearn, B.C.,Jr., Eby, G.N. (2014) Continent-scale linearity of kimberlite–carbonatite magmatism, mid-continent North America, *Earth and Planetary Science Letters*, 403, 1-14.

Eggler D.H. (1978) The effect of CO_2 upon partial melting of peridotite in the system Na_2O-CaO-Al_2O_3-MgO-SiO_2- CO_2 to 35 kb, with an analysis of melting in a peridotite-H_2O-CO_2 system, *American Journal of Science*, 278, 305-434.

Eggler D.H. (1987) Discussion of recent papers on carbonated peridotite, bearing on metasomatism and magmatism: an alternative. *Earth and Planetary Science Letters*, 82, 398-400.

Frezzotti, M.-L., Thouret, J.L.R. (2014) CO_2, carbonate-rich melts, and brines in the mantle, *Geoscience Frontiers*, 5, 697-710.

Gorman, P.J., Kerrick, D.M., Conolly, J.A.D. (2006) Modeling open system metamorphic decarbonation of subducting slabs, *Geochemistry Geophysics Geosystems*, 7, 4.

Guo, X., Yoshino, T., Katayama, I. (2011) Electrical conductivity anisotropy of deformed talc rocks and serpentinites at 3 GPa, *Physics of the Earth and Planetary Interiors*, 188, 69–81.

Hammouda, T., Chantel, J., Manthilake, G., Guignard, J., Crichton, W. (2014) Hot mantle geotherms stabilize calcic carbonatite magmas up to the surface, *Geology*, 42, 911-914.

Hammouda T., Laporte D. (2000) Ultrafast mantle impregnation by carbonatite melts, *Geology*, 28, 283-285.

Hammouda T., Keshav S. (2015) Melting in the mantle in presence of carbon; review of experiments and discussion on the origin of carbonatites, *Chemical Geology*, 418, 171-188.

Hanfland, M., Beister, H., Syassen, K., (1989) Graphite under pressure: equation of state and first-order Raman modes, *Physical Review B*, 39, 12598–12603.

Hauri, E. H., Shimizu, N., Dieu, J. J., and Hart, S. R., 1993, Evidence for hotspot-related carbonatite metasomatism in the oceanic upper mantle, *Nature*, 365, 221–227.

Hunter R.S., McKenzie D. (1989) The equilibrium geometry of carbonate melts in rocks of mantle composition, *Earth and Planetary Science Letters*, 92, 347-356.

Jackson, C.R.M., Parman, S.W., Kelley, S.P., Cooper, R.F. (2013) Noble gas transport into the mantle facilitated by high solubility in amphibole, *Nature Geosc*. 6, 562-565.

Kelemen, P.B, Manning, C.E. (2015) Reevaluating carbon fluxes in subduction zones, what goes down, mostly comes up, *Proceedings of the National Academy of Science*, 112, E3997-E4006.

Kono, Y., Kenney-Benson C., Hummer D., Ohfuji H., Park C., Shen G., Wang Y., Kavner A., Manning C.E. (2014) Ultralow viscosity of carbonate melts at high pressures, *Nature Communications*, 5, 5091.

Liu, J., Hirano, N., Machida, S., Xia, Q., Tao, C., Liao, S., Liang, J., Li, W., Yang, W., Zhang, G., Ding, T. (2020) Melting of recycled ancient crust responsible for the Gutenberg discontinuity, *Nature Communications*, 11:172.

Machida, S., Kogiso, T., Hirano, N. (2017) Petit-spot as definitive evidence for partial melting in the asthenosphere caused by CO_2, *Nature Communications*, 8:14302.

Martin, A.M., Hammouda, T. (2011) Role of iron and reducing conditions on the stability of dolomite + coesite between 4.25 and 6 GPa – a potential mechanism for diamond formation during subduction, *European Journal of Mineralogy*, 23, 5-16.

Molina, J.F., and Poli S. (2000) Carbonate stability and fluid composition in subducted oceanic crust: an experimental study on H_2O-CO_2-bearing basalts, *Earth and Planetary Science Letters*, 176, 295-310.

Næraa, T, Scherstén A, Rosing M.T., Kemp A.I.S., Hoffmann J.E, Kokfelt T.F, Whitehouse M.J. (2012) Hafnium isotope evidence for a transition in the dynamics of continental growth 3.2 Gyr ago, *Nature* 485, 627-630.

Nutman, A.P., Bennett, V.C., Friend C.R.L., Van Kranendonk, M.J., Chivas, A.R. (2016) Rapid emergence of life shown by discovery of 3,700-million-year-old microbial structures, *Nature* doi:10.1038/nature19355.

Petricek, V., Dusek, M., and Palatinus, L. (2006) Jana2006. The Crystallo- graphic Computing System, Institute of Physics, Prague.

Poli, S, Schmidt, M.W. (1995) H2O transport and release in subduction zones: Experimental constraints on basaltic and andesitic systems, *Journal of Geophysical Research*, 100, 22299-22314.

Roedder, E. (1965) Liquid CO_2 inclusions in olivine-bearing nodules and phenocrysts from basalts, *American Mineralogist*, 50, 1746-1782.

Scambelluri, M, Bebout, G.E., Belmonte, D., Gilio, M., Campomenosi, N., Collins, N., Crispini, L. (2016) Carbonation of subduction-zone serpentinite (high-pressure ophicarbonate;

297 Ligurian Western Alps) and implications for the deep carbon cycling, *Earth and*
298 *Planetary Science Letters*, 441, 155-166.

299 Schmerr N. (2012) The Gutenberg Discontinuity: Melt at the Lithosphere-Asthenosphere
300 Boundary, *Science*, 335, 1380-1383.

301 Schmidt, M.W., Poli, S (1995) Experimentally based water budgets for dehydrating slabs and
302 consequences for arc magma generation, *Earth and Planetary Science Letters*, 163, 361-
303 379.

304 Sifré, D., Gardés, E., Massuyeau, M., Hashim, L., Hier-Majumder, S., Gaillard, F. (2014)
305 Electrical conductivity during incipient melting in the oceanic low-velocity zone, *Nature*,
306 509, 81-85.

307 Sleep, N.H. (2009) Stagnant lid convection and carbonate metasomatism of the deep continental
308 lithosphere, *Geochememistry Geophysics Geosystems* 10:Q11010.

309 Sleep, N.H., Bird, D.K., Pope, E. (2012) Paleontology of Earth's Mantle, *Annual Review of*
310 *Earth and Planetary Science*, 40, 277–300.

311 Soyer, W., Unsworth, M. (2006) Deep electrical structure of the northern Cascadia (British
312 Columbia, Canada) subduction zone: Implications for the distribution of fluids, *Geology*
313 34, 53-56.

314 Stagno, V., Ojwang, D.O., McCammon, C.A., Frost, D.J. (2013) The oxidation state of the
315 mantle and the extraction of carbon from Earth's interior, *Nature* 493, 84-88.

316 Syracuse E.M., van Keken P.E., Abers G.A. (2010) The global range of subduction zone thermal
317 models, *Physics of the Earth and Planetary Interiors*, 183, 73-90.

318 Watson EB, Brennan JM, Baker DR (1990) Distribution of fluids in the continental mantle. In:
319 Mezies MA (ed) Continental Mantle, Clarendon Press, Oxford, pp 111-125.

320 Zhang G-L, Chen l-H, Jackson M G, Hofmann A W, Evolution of carbonated melt to alkali
321 basalt in the South China Sea, *Nature Geoscience* 10, 229–235 (2017).

322 Zhang Y, Zindler A (1993) Distribution and evolution of carbon and nitrogen in *Earth and*
323 *Planetary Science Letters*, 117, 331-345.

324
325

326

327 **Figure 1.** Pressure – temperature path followed during the compression melting experiment.
328 Phase relationships in the synthetic CaO-MgO-SiO_2+CO_2 system (solid red lines) drawn after
329 (Eggler, 1978). Univariant reactions are labeled according to the list displayed in the top left-
330 hand corner. Diamond symbols represent P – T conditions where phases have been identified,
331 using in-situ X-ray diffraction. Squares with numbers inside represent P – T conditions where
332 mineral transformations have been observed. Phase-in indicates that new diffraction peaks have
333 been observed, corresponding to the phase in question (except for melt). Arrows indicates
334 decrease or increase in diffraction line intensities of the corresponding phases. Melting is
335 deduced from these variations, as discussed in the main text, and confirmed by imaging of
336 quenched textures (see Fig.3). Major phase fields are indicated by underlined and italicized
337 labels. Abbreviations are: dol = dolomite; en = enstatite; di = diopside; fo = forsterite; V = vapor
338 (CO_2); L = carbonate melt.
339

340

341 **Figure 2.** X-ray diffraction patterns recorded during the experiment. Units of x-ray intensity on
342 the count abscissa are arbitrary (a.u.) and patterns are offset vertically for clarity. Pressure and
343 temperature conditions are given for each pattern. Diagnostic diffraction lines for minerals are
344 indicated with arrows. Each pattern corresponds to a diamond symbol of Figure 1. Highlighted
345 patterns (in red) are evidence for decarbonation and melting.

346
347

348

349 **Figure 3.** Scanning electron images of the quenched experiment illustrating the processes
350 involved in compression melting. (A) Texture resulting from the decarbonation reaction dolomite
351 + enstatite = diopside + forsterite + vapor. The presence of vapor is attested by the vacuoles
352 (arrows) surrounded by rims consisting of an intergrowth of diopside and forsterite. (B) Texture
353 resulting from the melting reaction diopside + forsterite + CO_2 = enstatite + melt, producing a
354 carbonatitic liquid. The melt is disseminated at grain boundaries, throughout the sample.
355 Abbreviations are the same as those used in Figure 1, except for Carbo-Melt=quenched melt of
356 carbonatitic composition.

357
358

Figure 4. Summary of the proposed mechanism for the introduction and dissemination of carbonate melts. (A) Carbonate melts produced by compression melting in front of the subducting slab occur at depth between 100 and 150 km (yellow patch beneath the arc region). The region for stable carbonatite melt (in light green) is bounded by the Lithosphere-Astenosphere Boundary, where decarbonation occurs (LAB, dotted red line), on top, and the redox front controlled by the EMOD/G equilibrium, below which the stable form of carbon is graphite/diamond (dotted green line). Yellow arrows illustrate carbonatite migration away from the subduction zone. Other yellow patches indicate region of carbonatite implication in magmatism, such as spreading centers and hot spots (B), and petit spots (C). Vertical red thick arrows represent oceanic magmatism where carbonate melts participate and may be extracted. In panel (C), note that carbonate melt present at the back of the subducting plate can be introduced to greater depth. Vertical blue thick arrows represent arc magmatism, with implication of water-dominated fluids. Abbreviations are: dol = dolomite; en = enstatite; di = diopside; ol = olivine, mst = magnesite.

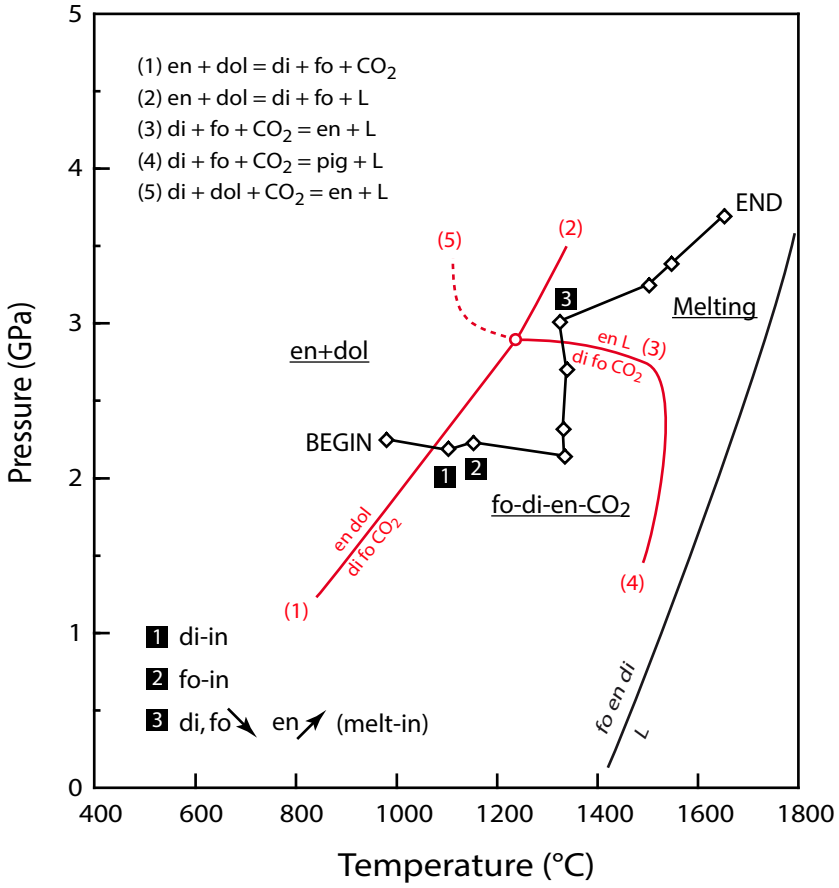
(1) en + dol = di + fo + CO_2
(2) en + dol = di + fo + L
(3) di + fo + CO_2 = en + L
(4) di + fo + CO_2 = pig + L
(5) di + dol + CO_2 = en + L
END
Melting
(5)
(2)
3
en L (3)
di fo CO_2
en+dol
BEGIN
1
2
fo-di-en-CO_2
en dol
di fo CO_2
(1)
(4)
1 di-in
2 fo-in
3 di, fo ↘ en ↗ (melt-in)
fo en di
L
Pressure (GPa)
Temperature (°C)
0
1
2
3
4
5
400
600
800
1000
1200
1400
1600
1800

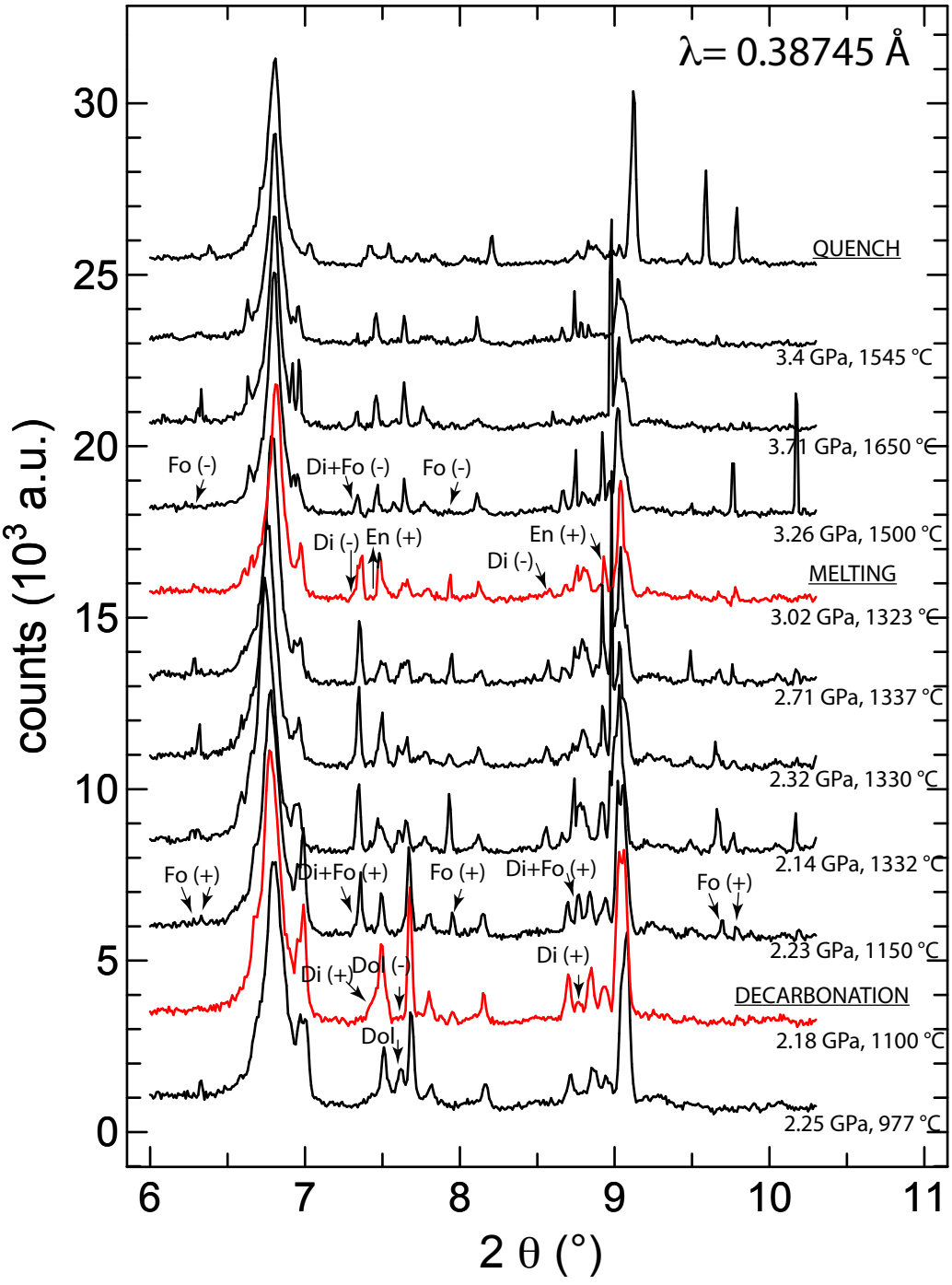
λ= 0.38745 Å
counts (10³ a.u.)
2 θ (°)
QUENCH
3.4 GPa, 1545 °C
3.71 GPa, 1650 °C
3.26 GPa, 1500 °C
MELTING
3.02 GPa, 1323 °C
2.71 GPa, 1337 °C
2.32 GPa, 1330 °C
2.14 GPa, 1332 °C
2.23 GPa, 1150 °C
DECARBONATION
2.18 GPa, 1100 °C
2.25 GPa, 977 °C
Fo (-)
Di+Fo (-)
Fo (-)
Di (-)
En (+)
En (+)
Di (-)
Fo (+)
Di+Fo (+)
Fo (+)
Di+Fo (+)
Fo (+)
Di (+)
Dol (-)
Di (+)
Dol

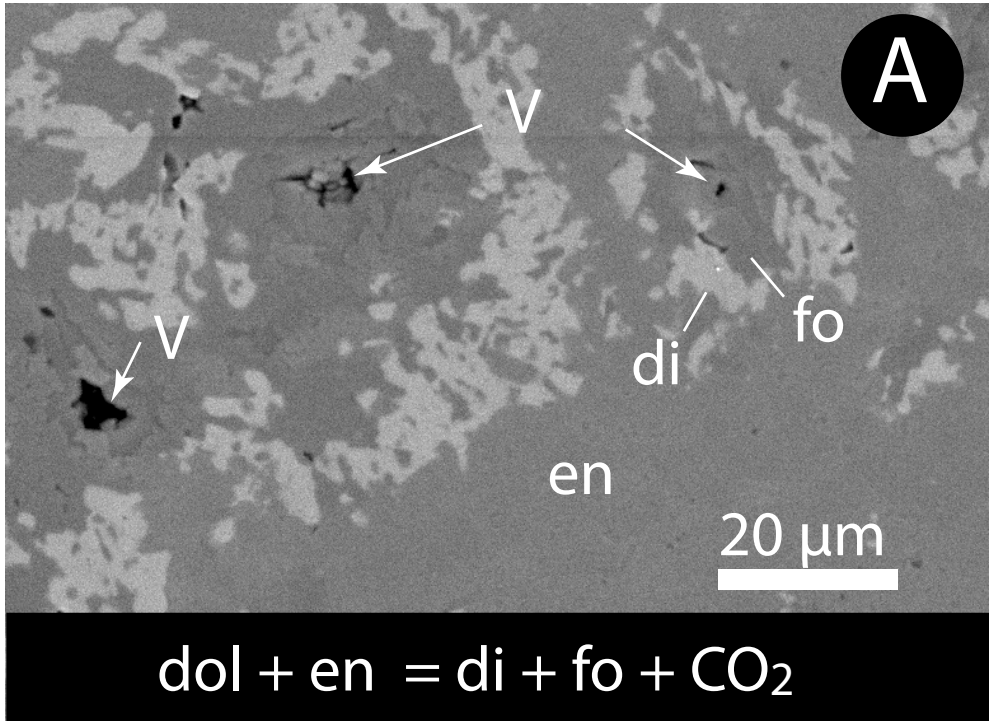
A
V
V
di
fo
en
20 µm
dol + en = di + fo + CO2

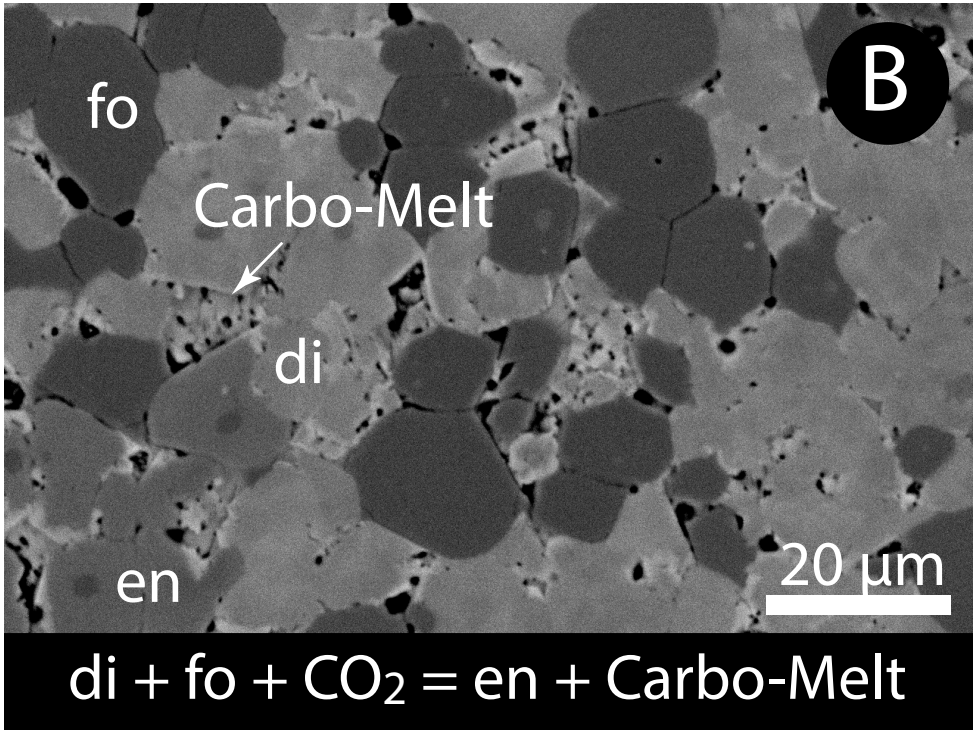
B
fo
Carbo-Melt
di
en
20 µm
di + fo + CO2 = en + Carbo-Melt

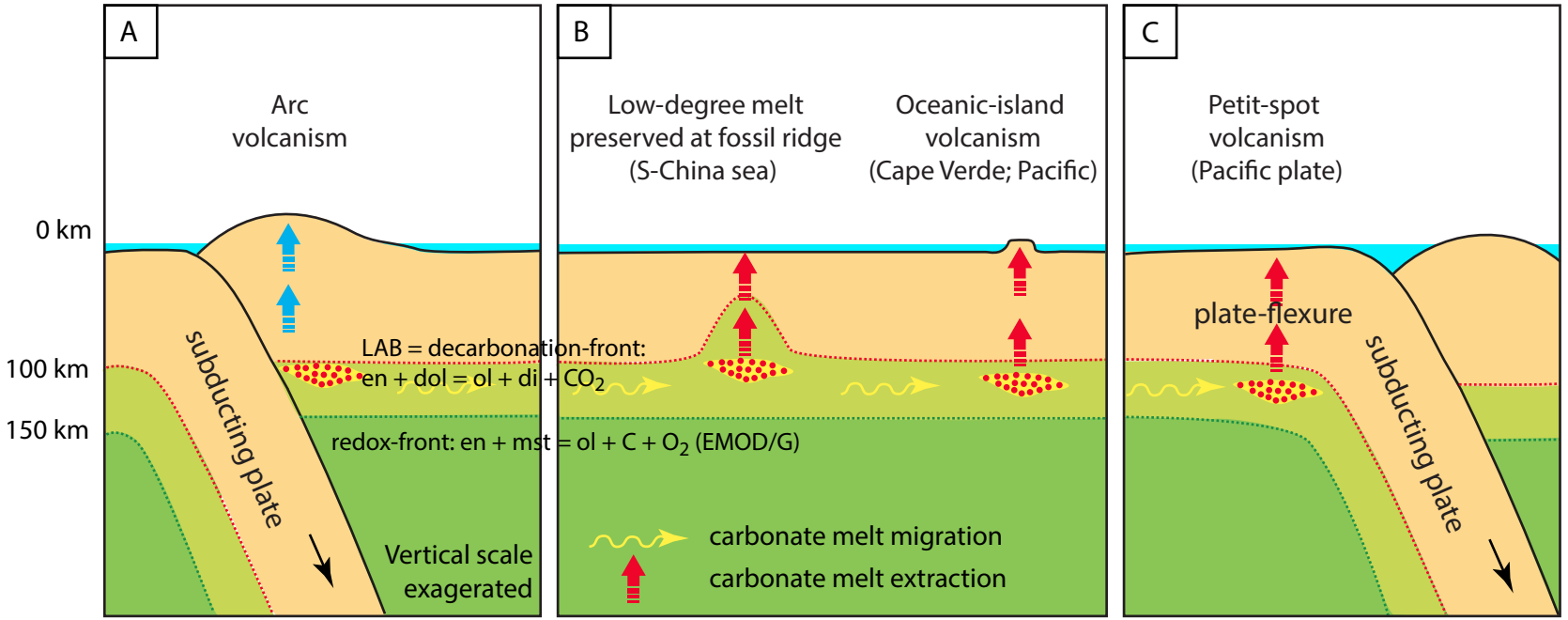
A
Arc
volcanism
B
Low-degree melt
preserved at fossil ridge
(S-China sea)
Oceanic-island
volcanism
(Cape Verde; Pacific)
C
Petit-spot
volcanism
(Pacific plate)
0 km
100 km
150 km
LAB = decarbonation-front:
en + dol = ol + di + CO_2
redox-front: en + mst = ol + C + O_2 (EMOD/G)
subducting plate
Vertical scale
exagerated
carbonate melt migration
carbonate melt extraction
plate-flexure
subducting plate

Refueling the mantle carbon by compression melting

Tahar HAMMOUDA[1], Geeth MANTHILAKE[1], Philippe GONCALVES[2], Julien CHANTEL[1,3*], Jérémy GUIGNARD[4**], Wilson CRICHTON[4], Fabrice GAILLARD[5]

Supplementary material: Methods

High-pressure experiment design

Experiments were performed using the 2000 ton multianvil press operated on ID06 beam line of the European Synchrotron Radiation Facility, following the approach used in Hammouda et al. (2014). The difference from quench experiments is that several data points were collected during the same experiment. The conditions investigated are shown on Figure 1 (main text). As pressure and temperature were varied, the phases present in the experiment were identified using X-ray diffraction (see below).

In order to introduce CO_2 and have it react with mantle mineral assemblage a mixture of natural dolomite (DNY, Hammouda et al. (2014)) and synthetic enstatite was used. Heating of dolomite + enstatite at pressure below 2.7 GPa produces CO_2 vapor phase, according to the reaction decarbonation reaction:

$$\text{Enstatite} + \text{Dolomite} = \text{Diopside} + \text{Forsterite} + CO_2.$$

This reaction has been studied, together with other important reactions in the peridotite + CO_2 synthetic system (Eggler, 1978), as illustrated in Figure 1 (main text). Formation of

diopside and forsterite by the decarbonation reaction yielded phases that are involved in peridotite + CO_2 melting (see Figure 1 of main text).

The starting mixtures were loaded in graphite capsules. The samples were compressed using 18-mm edge length Cr-doped MgO octahedra as pressure transmitting media that were squeezed with 11 mm edge length tungsten carbide anvils (18/11 assembly). Heating was performed using a stepped graphite furnace. The sample temperature was determined using a W-Re (5-26) thermocouple that was separated from the graphite capsule by a thin MgO disk. No correction was applied for the effect of pressure on the e.m.f. Pressure was determined using the cell parameters of the graphite capsule material and the equation of state of Hanfland et al. (1989). Error on temperature and pressure are considered to be about 50 °C and 0.2 GPa, respectively. No water was added to the starting material. The experiment is therefore considered to be nominally anhydrous, although we cannot exclude the presence of small quantities of adsorbed water in the starting material.

X-ray data collection

We used in situ X-ray diffraction for phase identification at high pressure and high temperature. Monochromatic X-ray diffraction patterns (λ=0.38745 Å) were collected with a Tl:NaI Bicron scintillator detector, scanning on a large-radius pseudorotation over a 2θ angular range 6-11°, with step size 0.01°. Two sets of adjustable slits were used to define the volume of the diffracting sample, and remove diffraction signal from the up- and downstream gaskets and furnace. Angular calibration of the instrument was performed before the experiment against NIST standard LaB_6 SRM660a. X-ray diffraction patterns were processed by full profile LeBail refinements with the Jana2006 software package (Petricek et al., 2006).

Chemical analysis of the quenched phases

After quenching, the phase assemblage was characterized using a JEOL JSM-5910LV scanning electron microscope operating at 15 kV. Quantitative analyses of the quenched phases were performed using a CAMECA SX100 electron microprobe. Accelerating voltage was 15 kV and probe current on the Faraday cup was 15 nA. We used focused beam for minerals and defocused beam for quenched melts. In the latter case, beam diameter depended on the size of quenched melt pockets (usually, a few micrometers), and beam damage is difficult to avoid. The following standards were used: wollastonite for Ca and Si, olivine for Mg, magnetite for Fe. Carbon was determined by stoichiometry for the carbonates, and it was estimated by difference to 100% on analysis total for the quenched melt, and by stoichiometry, assuming that all cations (except Si) are bound to carbonate. As can be seen in **Table ST1**, the agreement between of the two methods is satisfactory (within 5% relative), given the difficulty in analyzing small quenched carbonate melt pools.

Electron microprobe analyses of quenched phases are displayed in **Table ST1**. Forsterite has end-member composition, while enstatite contains a slight amount of calcium (about 0.1 atom per formula unit, on the basis of 6 oxygen atoms). Two clinopyroxene types are found. One is close to diopside composition, while the other is of pigeonite type. We note that the diopside-like pyroxene is deficient in Ca, with 1.33 Mg and 0.74 Ca atoms per formula unit. This deficit can be attributed either to Ca partitioning in the melt (melt has Ca/(Ca+Mg) > 1, see **Table ST1**) or in the vapor phase, as suggested by Martin and Hammouda (2011). Melt composition varies among the different analytical spots. Variations are found for SiO_2 content and for Ca / (Ca+Mg) atomic ratios (Ca#). Given the difficulty encountered while analyzing the quenched melt, it is not clear whether this observation reflects true compositional zoning, contamination by adjacent silicate minerals during analysis, or modification during quenching. In the absence of large separated quenched melt pools, it is not possible to

conclude on the effect of quenching, in the manner discussed by Dalton and Presnall (1998). For the purpose of the present investigation, the key point is that melts are carbonatitic.

Supplementary references

Dalton J.D., Presnall D.C. (1998) Carbonatitic melts along the solidus of model lherzolite in the system CaO-MgO-Al_2O_3-SiO_2-CO_2 from 3 to 7 GPa, Contrib. Mineral. Petrol. 131, 123-135.

Eggler D.H. (1978) The effect of CO_2 upon partial melting of peridotite in the system Na_2O-CaO-Al_2O_3-MgO-SiO_2- CO_2 to 35 kb, with an analysis of melting in a peridotite-H_2O-CO_2 system, Am. J. Sci. 278, 305-434.

Hammouda, T., Chantel, J., Manthilake, G., Guignard, J., Crichton, W. (2014) Hot mantle geotherms stabilize calcic carbonatite magmas up to the surface, Geology 42, 911-914.

Hanfland, M., Beister, H., Syassen, K., (1989) Graphite under pressure: equation of state and first-order Raman modes, Phys. Rev. B, v. 39, p. 12598–12603.

Martin, A.M., Hammouda, T. (2011) Role of iron and reducing conditions on the stability of dolomite + coesite between 4.25 and 6 GPa – a potential mechanism for diamond formation during subduction, Eur. J. Mineral. 23, 5-16.

Petricek, V., Dusek, M., and Palatinus, L., 2006, Jana2006. The Crystallo- graphic Computing System, Inst. of Phys., Prague.

Supplementary Table

Table 1: Average phase composition obtained by electron microprobe analysis.

phase[a]	opx (2)[b]	cpx ? (1)	pig (2)	fo (2)	melt (8)
SiO_2	60.0 (0.1)[c]	53.17	58.8 (0)	43.3 (0.6)	1.3 (0.7)
FeO	0.02 (0.01)	0.02	0.01 (0.01)	0.04 (0.01)	0.04 (0.02)
MgO	37.8 (0.6)	24.06	32.0 (0.5)	56.5 (0.2)	10.1 (1.3)
CaO	2.69 (0.27)	18.71	9.69 (0.50)	0.40 (0.04)	45.0 (1.8)
CO_2 by diff[d]					44.0 (0.8)
CO_2 by stoich[e]					46.3 (1.4)
Total	100.6	95.95	100.5	100.2	[f]
atoms per formula unit[g]					
Si	2.01 (0.01)	1.97	2.01 (0)	1.01 (0.01)	
Fe	0.0 (0)	0.00	0.0 (0)	0.0 (0)	
Mg	1.89 (0.03)	1.33	1.63 (0.02)	1.97 (0.02)	
Ca	0.10 (0.01)	0.74	0.35 (0.02)	0.01 (0.00)	
Ca#[h]	0.05 (0.01)	0.36	0.18 (0.01)	0.01 (0.00)	0.76 (3)

Notes:
[a]phase abbreviations are: opx=orthopyroxene, cpx?=clinopyroxene not confirmed, pig=pigeonite (Ca-poor clinopyroxene), fo=forsterite, melt=quenched carbonatitic melt.
[b]number in brackets indicated the number of analyses performed for each phase.
[c]number in bracket next to composition indicates 1 standard deviation.
[d]CO_2 calculated by difference to 100%, using the sum of the other oxides.
[e]CO_2 calculated by stoichiometry, assuming that all cations (except Si) are bound to carbonate.
[f]no total is given because CO_2 is not directly analyzed.
[g]atoms per formula units are calculated assuming the following number of oxygen: pyroxene=6, forsterite=4.
[h]Ca# = Ca / (Ca+Fe+Mg) in atoms.